Supporting Information

Anion Exchange of a Cationic Cd(II)-based Metal-Organic Framework with potassium ferricyanide towards highly active Fe_3C-containing Fe/N/C catalysts for Oxygen Reduction

Jia-Wei Huang, ‡[a] Yu-Bin Chen, ‡[b] Xiao Liu, [b] Yi-Chen Huang, [a] Ye-Lin Ding, [a] Yang Xu, [a] Hong-Chang Yao, [c] Hai-Bin Zhu *[a] and Hui Yang *[b]

[a] School of Chemistry and Chemical Engineering, Southeast University, Nanjing, 211189, China, email: zhuhaibin@seu.edu.cn

[b] Shanghai Advanced Research Institute, Chinese Academy of Sciences, Shanghai, 201210, China, email: yangh@sari.ac.cn

[c] College of Chemistry and Molecular Engineering, Zhengzhou University, Zhengzhou, 450002, China

Experimental Section

Materials and methods

All the reagents and solvents were commercially available and used as received. Cd-TTPBA-4 ligand was obtained according to our reported method.[1] FT-IR spectra were collected on a Thermo Scientific Nicolet 5700 FT-IR spectrophotometer with KBr pellets in the 400-4000 cm^{-1} region. UV-Vis absorption spectra were measured using a Shimadzu UV-2450 spectrophotometer. Scanning electron microscopy (SEM) images were obtained by the FEI Inspect F50 system. Transmission Electron Microscopy (TEM), High-Resolution Transmission Electron Microscopy (HRTEM) and elemental mapping were performed on a JEOL JEM-2100F field emission electron microscope. The high-angle annular dark field scanning TEM (HAADF-STEM) images were obtained by FEI Titan Themis G2 60-300. Powder X-ray diffraction (PXRD) data were recorded on XRD diffractometer Ultima IV, Rigaku Corporation) with Cu-Kα radiation (λ = 1.54056 Å). The Brunauer-Emmett-Teller

(BET) surface area and pore distribution were measured by nitrogen adsorption-desorption on a Micromeritics ASAP 2020 surface area and porosity analyzer. Raman spectra were recorded on a Thermo DXR 532 Raman spectrometer (USA) with a laser excitation wavelength of 532 nm. X-ray photoelectron spectroscopy (XPS) was carried out on a Thermo Scientific Spectrometer with an Escalab 250 Xi X-ray as the excitation source, referenced to C 1s binding energy (BE) of 284.45 eV. The actual loadings of Fe in the samples were measured by ICP-OES (SHIMADZU, ICPE-9000).

Synthesis of Cd-TTPBA-4

Cd-TTPBA-4 crystals were synthesized according to our previous literature.[1] A mixture of $Cd(ClO_4)_2 \cdot 6H_2O$ (33.6 mg, 0.08 mmol) and **TTPBA-4** (13.6 mg, 0.02 mmol) were dissolved in 9 mL of DMF-H_2O-CH_3CH_2OH (in 1:1:1 volume ratio), and sealed in a Teflon-lined autoclave (25 mL). The mixture was heated at 100 ^oC for 3 days. Upon cooled to room temperature at a rate of 5 ^oC/h, Light yellow crystals were collected in 60% yield (based on **TTPBA-4** ligand). IR (KBr, cm^{-1}): 3422.6 (m), 3110.9 (w), 2970.9 (w), 1596.6(m), 1516.2 (vs), 1315.6 (m), 1271.4 (m), 1095.0 (s), 833.5 (w), 628.2 (w), 545.4 (w). Calcd for $CdC_{45}H_{59}ClN_{16}O_{16}$: C, 44.02; H, 4.84; N, 18.25. Found: C, 44.11; H 4.89, N, 18.31.

Preparation of $\{K_2[Fe(CN)_6]\}^-$**@Cd-TTPBA-4**-X

The absorbances of the standard potassium ferricyanide working solutions C_1–C_5 (10^{-4}, 3×10^{-4}, 6×10^{-4}, 9×10^{-4}, 1×10^{-3} mol L^{-1}) were measured by UV–vis and the values obtained were A_1–A_5. The calibration line was constructed with the following equation:

$$A_i = b_0 + b_1 \times C_i$$

where b_0 is the intercept of the calibration line (-0.0214) and b_1 (L mol^{-1}) is the slope of the calibration line (1.649 L mol^{-1}).

Crystals of **Cd-TTPBA-4** (20 mg, 0.0163 mmol) were soaked into aqueous solution containing equal molar potassium ferricyanide at different concentrations (1: 2.5×10^{-4} mol L^{-1}, 2: 5×10^{-4} mol L^{-1}, 3: 7.5×10^{-4} mol L^{-1}, 4: 10^{-3} mol L^{-1}) for 4 hour, and the adsorption of $\{K_2[Fe(CN)_6]\}^-$ was determined using a UV–vis spectrometer. The resultant crystals of $\{K_2[Fe(CN)_6]\}^-$**@Cd-TTPBA**-X （X represents concentration code） were filtered**,** washed with the distilled water and dried in the air. Inductively coupled plasma (ICP)

measurement of $\{K_2[Fe(CN)_6]\}^-$@**Cd-TTPBA**-2 revealed that the molar ratio of K/Fe was 1.7 : 1, which is close to 2:1. Accordingly, the exchanged anion should be in the form of $\{K_2[Fe(CN)_6]\}^-$ with one negative charge.

In order to confirm that it is ion exchange, the online UV-Vis absorption spectra show that the absorbed $\{K_2[Fe(CN)_6]\}^-$ can be gradually released from $\{K_2[Fe(CN)_6]\}^-$@**Cd-TTPBA-4** in the saturated $NaClO_4$ solution (Fig. S1), whereas this is not observed in the deionized water. It is obvious that the ClO_4^- ion enters into the channel of Cd-TTPBA-4 and releases the anion $\{K_2[Fe(CN)_6]\}^-$ by means of anion-exchange, which in turn testifies to the anion-exchange nature of $\{K_2[Fe(CN)_6]\}^-$ absorption with **Cd-TTPBA-4**.

The content of iron in $\{K_2[Fe(CN)_6]\}^-$@**Cd-TTPBA-4**-X after anion-Exchange was calculated using the mass balance according to equation:

$$Q_{Fe} = \frac{(C_0 - C)VM_{Fe}}{m}$$

where Q_{Fe} (wt%) is the adsorbed content, C_0 and C (mol L^{-1}) are the initial and the post-exchange concentrations, V (L) is the volume of solution, M_{Fe} (g mol^{-1}) is the relative atomic mass of iron, and m(g) is the mass of **Cd-TTPBA-4**.

Preparation of N-C and Fe/N/C electrocatalysts

The N-C and Fe/N/C electrocatalysts were prepared by the temperature-programmed pyrolysis of **Cd-TTPBA-4** and $\{K_2[Fe(CN)_6]\}^-$@**Cd-TTPBA-4**-X, respectively. Typically, 120 mg of **Cd-TTPBA-4** and $\{K_2[Fe(CN)_6]\}^-$@**Cd-TTPBA-4**-X was heated to the target temperature (800°C, 900°C, 1000°C or 1100°C) at a heating rate of 5°C min^{-1}. After reaching the target temperature, it was kept constant for 2 hours. The resultant samples were designated as N-C-T and Fe/N/C-T-X (T indicates the carbonization temperature).

Electrochemical measurements

Electrochemical measurements were performed on a CHI 604E workstation with a three-electrode cell system. In 0.1 M KOH solution, Pt wire and Ag/AgCl were used as the counter and reference electrodes, respectively. The potential difference between the Ag/AgCl reference electrode and reversible hydrogen electrode (RHE) is 0.92 V in O_2-saturated 0.1 M KOH electrolyte. In 0.1 M $HClO_4$ solution, graphite rod and $Hg/HgCl_2$ were used as the counter and reference electrodes, respectively. The potential difference

between the $Hg/HgCl_2$ reference electrode and reversible hydrogen electrode (RHE) is 0.29 V in O_2-saturated 0.1 M $HClO_4$ solution. Prior to use, the glass carbon rotating disk electrode (RDE, 3 mm in diameter) and rotating ring disk electrode (RRDE, SD: 0.2475 cm^2) were polished with 0.3 and 0.05 μm Al_2O_3 slurry, and washed in ultrapure-water and ethanol. The Fe/N/C catalyst loading was 0.6 mg cm^{-2} in both basic and acidic electrolyte. As comparison, the loading of commercial 20 wt % Pt/C was 0.2 mg cm^{-2}. The RDE and RRDE tests were conducted in O_2-saturated solution with a scan rate of 10 mV s^{-1} and at a rotating speed of 1600 rpm unless stated otherwise. Electrochemical impedance spectroscopy (EIS) measurements were performed by applying an AC voltage of 5 mV amplitude in a frequency range from 100 KHz to 100 mHz in 0.1 M KOH solution. The test was carried out at room temperature. The impedance data are fitted by the equivalent circuit of Randles model (Fig. S20). Error of fitting is less than $1.2*10^{-3}$. R_s is the sum of the electrode and electrolyte resistance values, C_{dl} is the double-layer capacity, R_{ct} is charge transfer resistance and Z_w is the Warburg impedance.

The methanol resistance was evaluated by comparing the CV before and after the addition of 2% CH_3OH to the O_2-saturated electrolyte. According to U.S. Department of Energy protocol, the accelerated durability tests (ADTs) were conducted by recording the LSV curves before and after the potential-cycling between 0.6 and 1.0 V (vs RHE) at a scan rate of 50 mV s^{-1} in O_2-saturated solution.

The Koutecky–Levich (K–L) equations can be obtained at various rotating speeds. The electron transfer number (n) can be calculated from the K–L equation:

$$\frac{1}{\mathrm{J}} = \frac{1}{J_L} + \frac{1}{J_K} = \frac{1}{BW^{1/2}} + \frac{1}{J_K}$$

$$B = 0.62nFC_0D^{2/3}V^{-1/6}$$

where J is the measured current density, J_K and J_L are the kinetic and limiting current densities, ω represents the angular velocity of the disk, n is the electron transfer number, F is the Faraday constant (96485 C mol^{-1}), C_0 is the bulk concentration of O_2 (1.2×10^{-6} mol cm^{-3}), D is the diffusion coefficient of O_2 in electrolytes (1.9×10^{-5} cm^2 s^{-1}) and V is the kinematic viscosity of the 0.1 M KOH (0.011 cm^2 s^{-1}) and 0.1 M $HClO_4$ (0.0089 cm^2 s^{-1}).

The H_2O_2 selectivity and the electron transfer number (n) can be calculated by the following equations:

$$H_2O_2\% = 200 \times \frac{\frac{I_r}{N}}{I_d + \frac{I_r}{N}}$$

$$n = 4 \times \frac{I_d}{I_d + \frac{I_r}{N}}$$

Here, N is the current collection efficiency (0.37) for the Pt ring. I_d and I_r are the disk and ring currents, respectively.

Zn–air batteries fabrication

The performance of the Zn–air battery was tested in a homebuilt electrochemical cell. The cathode was prepared by loading Fe/N/C-1000-2 catalyst on Teflon-coated carbon fiber paper (1.0 cm^2) with a catalyst loading of 1.0 mg cm^{-2}. Zn plate was used as the anode and 6.0 M KOH aqueous solution was used as the electrolyte. All the data were gathered on the as-fabricated cell at room temperature.

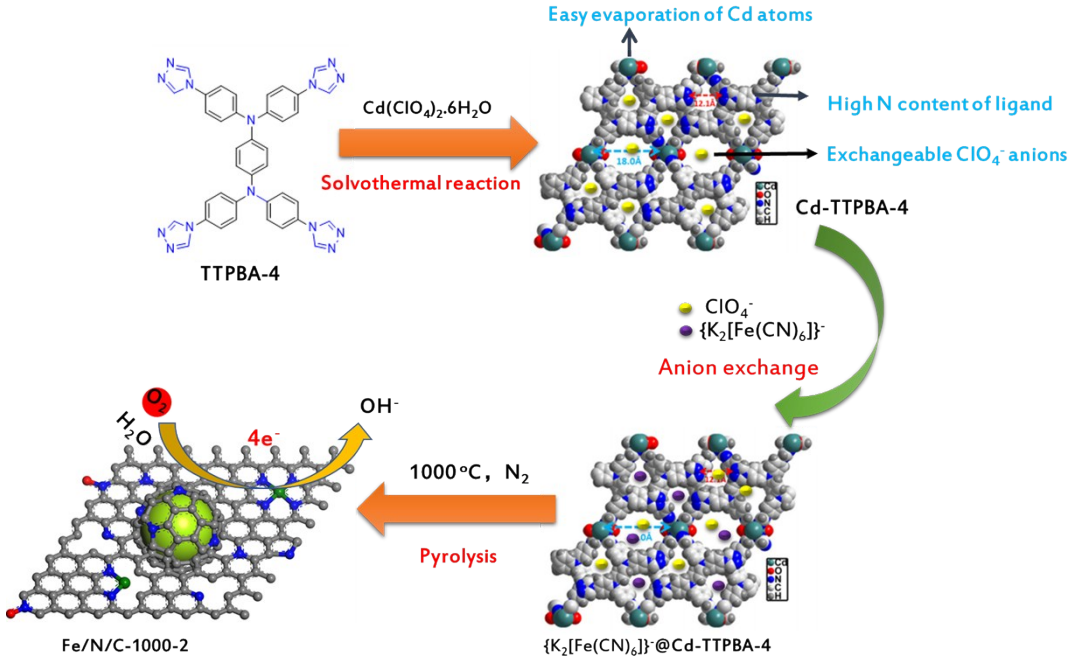

Scheme S1 Schematic illustration of preparation of Fe_3C-containing Fe/N/C catalyst.

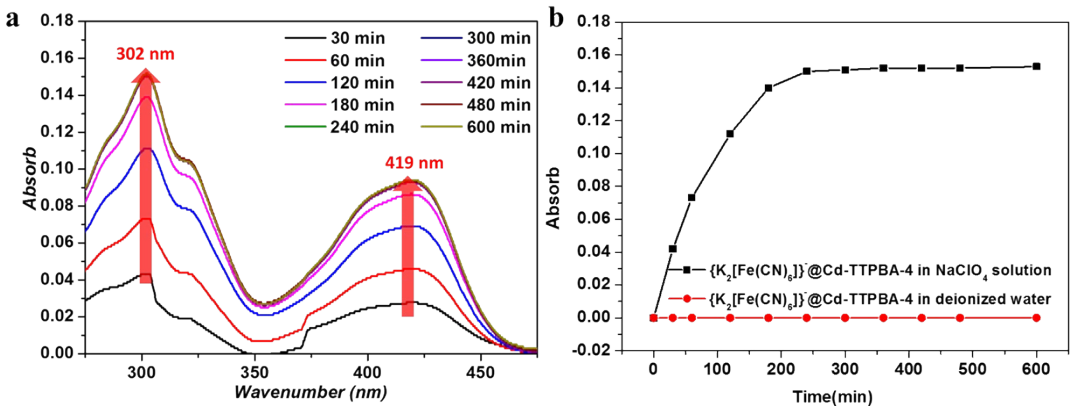

Fig. S1. (a) The UV-vis absorbance spectra of $\{K_2[Fe(CN)_6]\}^-$ release from $\{K_2[Fe(CN)_6]\}^-$@**Cd-TTPBA-4** in the saturated $NaClO_4$ solution. (b) comparison of the $\{K_2[Fe(CN)_6]\}^-$ release from $\{K_2[Fe(CN)_6]\}^-$@**Cd-TTPBA-4** in deionized water(red) and a saturated $NaClO_4$ solution (black).

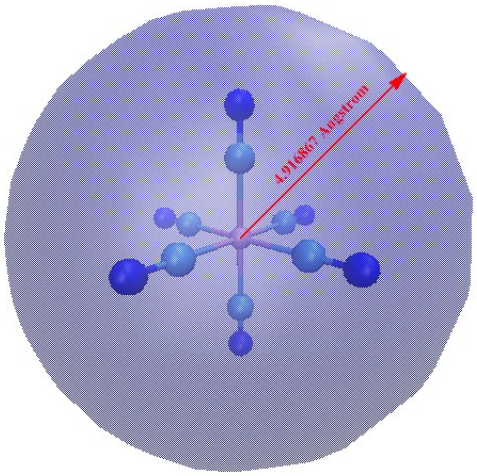

Fig. S2. The molecular volume and the distance from molecule center to electrostatic potential at surface vertices of $[Fe(CN)_6]^{3-}$ anions calculated by the Gaussian09 A02 suit. (All geometry optimizations were performed using the B3LYP functional within density functional theory (DFT) formalism and 6-31G(d, p) basis set was employed)

Table S1. Comparison of the iron content obtained by ICP and that obtained by UV-vis in $\{K_2[Fe(CN)_6]\}^-$@**Cd-TTPBA-4**-X

Sample	$C_{K_3[Fe(CN)_6]}$ /mol L^{-1}	Fe /wt%(ICP)	Fe /wt%(UV−vis)
$\{K_2[Fe(CN)_6]\}^-$@**Cd-TTPBA-4**-1	2.5×10^{-4}	0.37	0.39
$\{K_2[Fe(CN)_6]\}^-$@**Cd-TTPBA-4**-2	5×10^{-4}	0.42	0.45
$\{K_2[Fe(CN)_6]\}^-$@**Cd-TTPBA-4**-3	7.5×10^{-4}	0.49	0.48
$\{K_2[Fe(CN)_6]\}^-$@**Cd-TTPBA-4**-4	1×10^{-3}	0.60	0.61

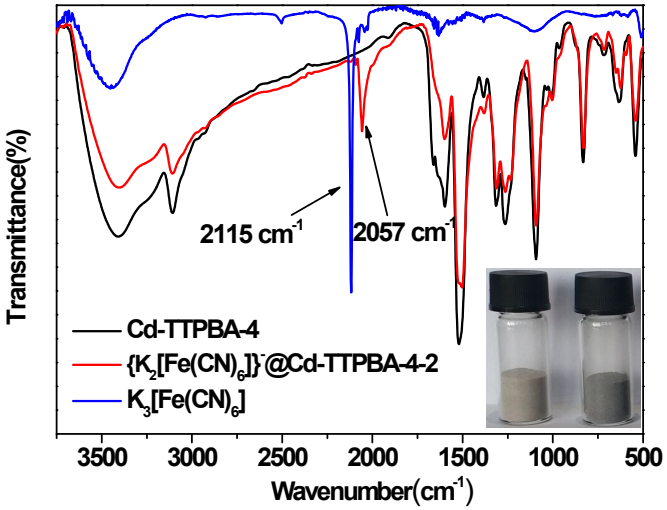

Fig. S3. FT-IR spectra of **Cd-TTPBA-4**, $\{K_2[Fe(CN)_6]\}^-$@**Cd-TTPBA-4**-2, $K_3[Fe(CN)_6]$ and Photographs of **Cd-TTPBA-4**, $\{K_2[Fe(CN)_6]\}^-$@**Cd-TTPBA-4**-2.

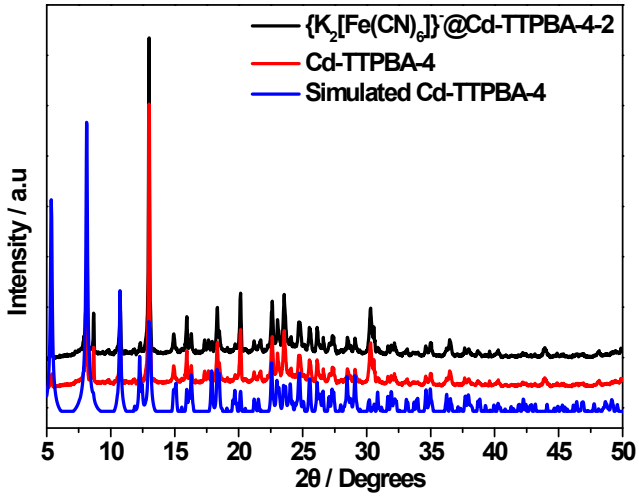

Fig. S4. Comparison of PXRD patterns of **Cd-TTPBA-4**, $\{K_2[Fe(CN)_6]\}^-$@**Cd-TTPBA-4**-2 and Simulated **Cd-TTPBA-4**.

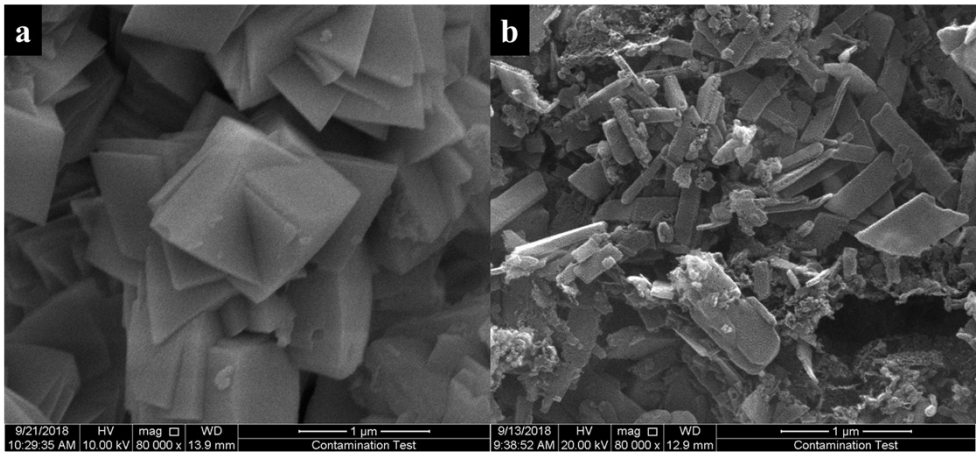

Fig. S5. SEM image of **Cd-TTPBA-4** and $\{K_2[Fe(CN)_6]\}^-$@ **Cd-TTPBA-4**-2.

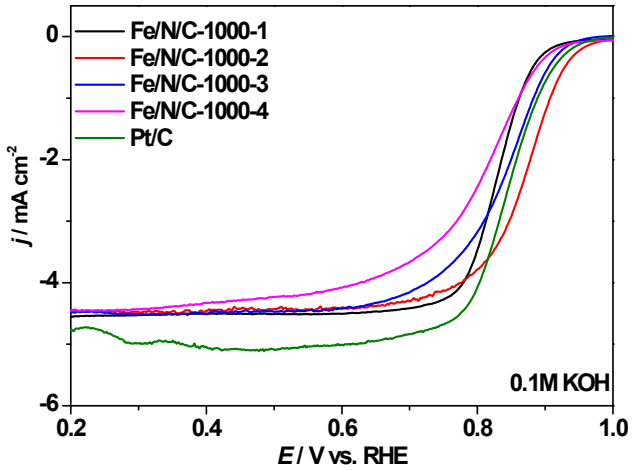

Fig. S6. LSV curves for Fe/N/C-1000-X in O_2-saturated 0.1M KOH at a rotation rate of 1600 rpm (X =1, 2, 3 and 4; X represents concentration code).

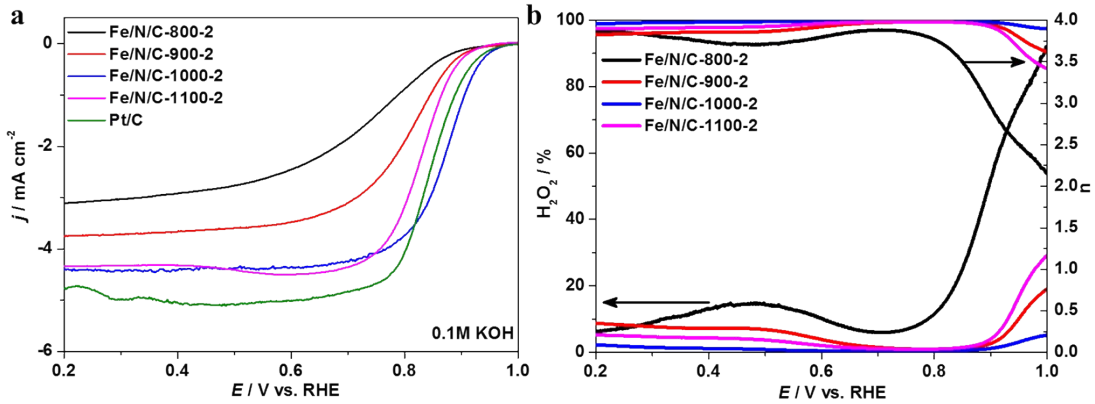

Fig. S7. (a) LSV curves for Fe/N/C-T-2 (T= 800, 900, 1000 and 1100) and Pt/C in O_2-saturated 0.1M KOH at a rotation rate of 1600 rpm; (b) Percentage of peroxide and electron transfer number of Fe/N/C-T-2 (T= 800, 900, 1000 and 1100) in O_2-saturated 0.1M KOH.

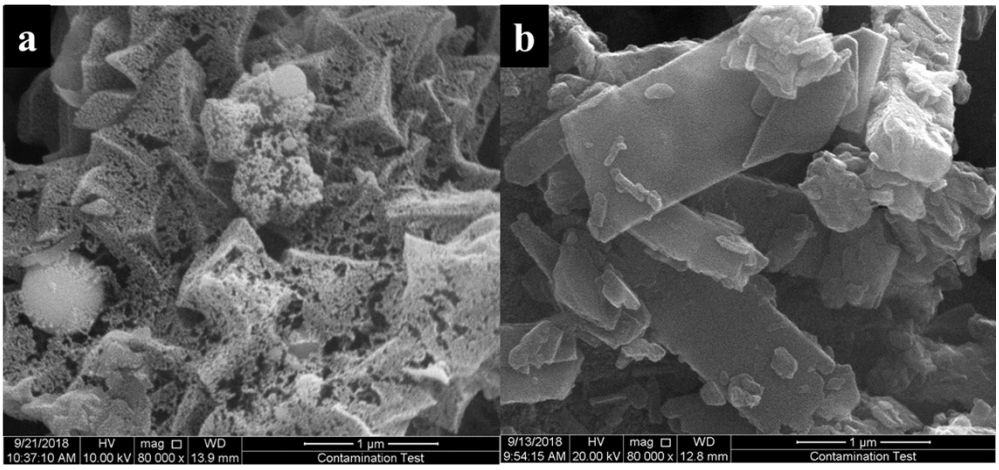

Fig. S8. SEM image of N-C-1000 and Fe/N/C-1000-2.

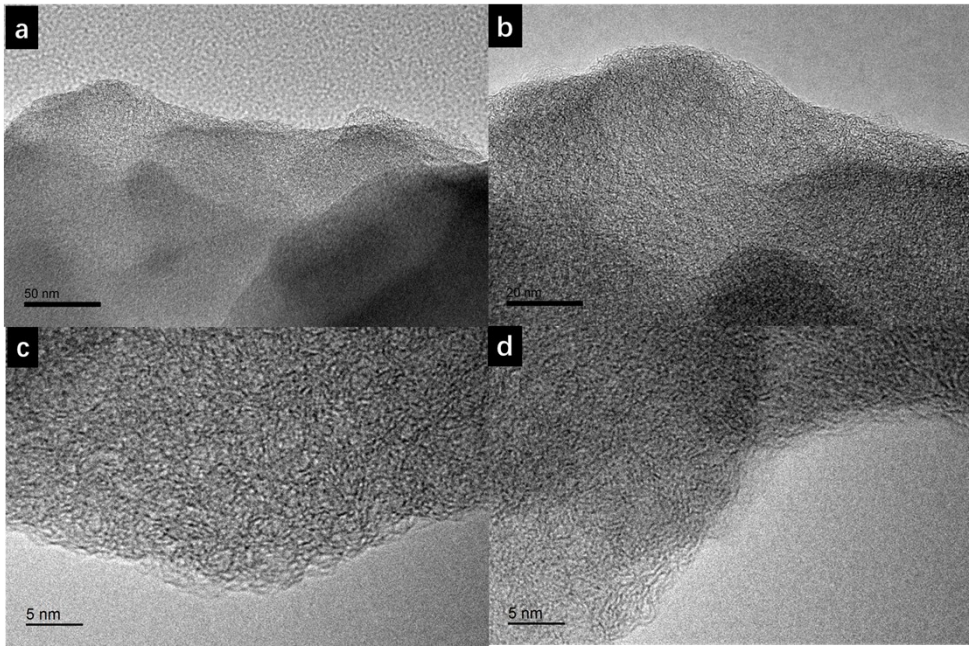

Fig. S9. HRTEM image of N-C-1000.

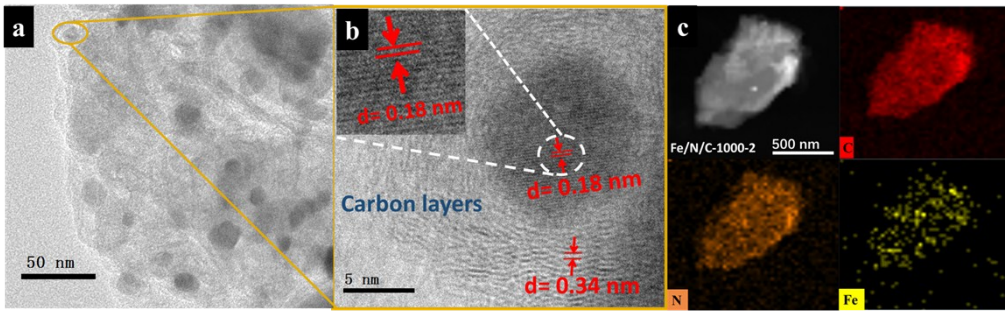

Fig. S10. (a and b) TEM and HRTEM images of Fe/N/C-1000-2**.** (c) HAADF-STEM image and the corresponding element mappings for C, N, Fe atoms of Fe/N/C-1000-2.

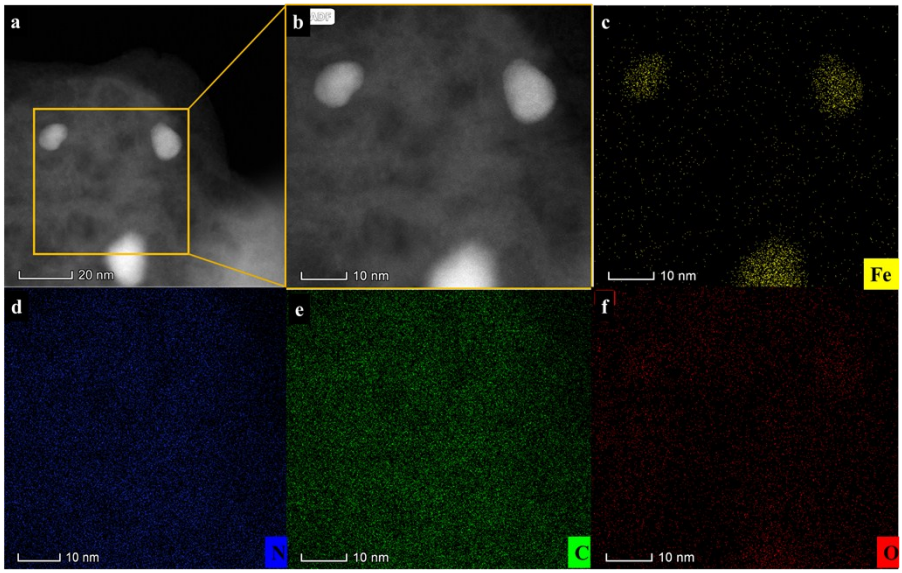

Fig. S11. (a and b) HAADF-STEM profile of Fe/N/C-1000-2. (c-f) HAADF-STEM EDS element mapping of Fe, N, C and O.

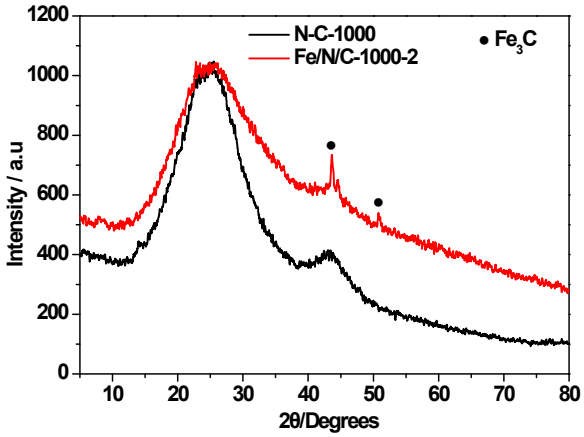

Fig. S12. PXRD patterns of N-C-1000 and Fe/N/C-1000-2.

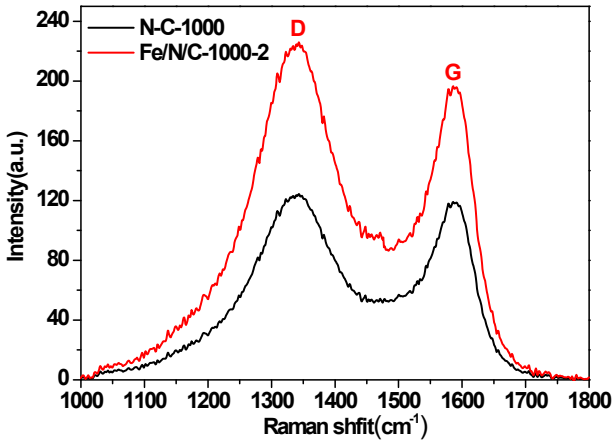

Fig. S13. Raman spectra of N-C-1000 and Fe/N/C-1000-2.

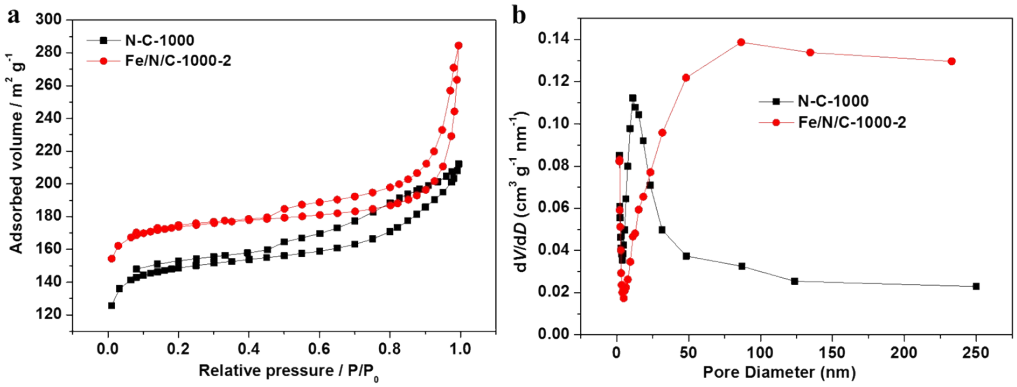

Fig. S14. (a) N_2 adsorption and desorption isotherms of N-C-1000 and Fe/N/C-1000-2; (b) Pore-size distributions of N-C-1000 and Fe/N/C-1000-2.

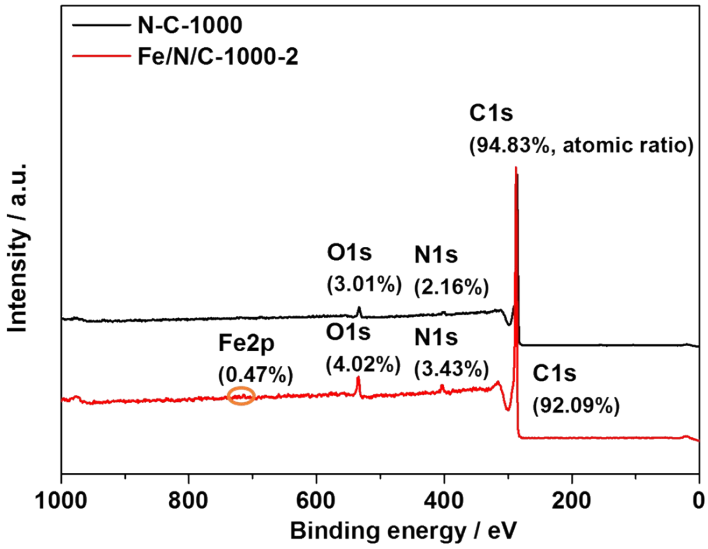

Fig. S15. XPS survey spectra of N-C-1000 and Fe/N/C-1000-2.

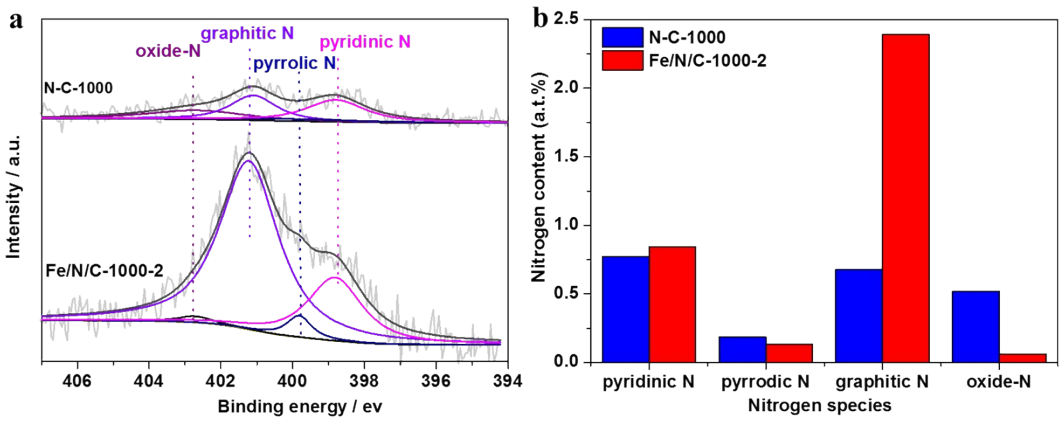

Fig. S16. (a) N 1s XPS spectra of N-C-1000 and Fe/N/C-1000-2 ; (b) N species percentage of N-C-1000 and Fe/N/C-1000-2 determined by XPS measurements.

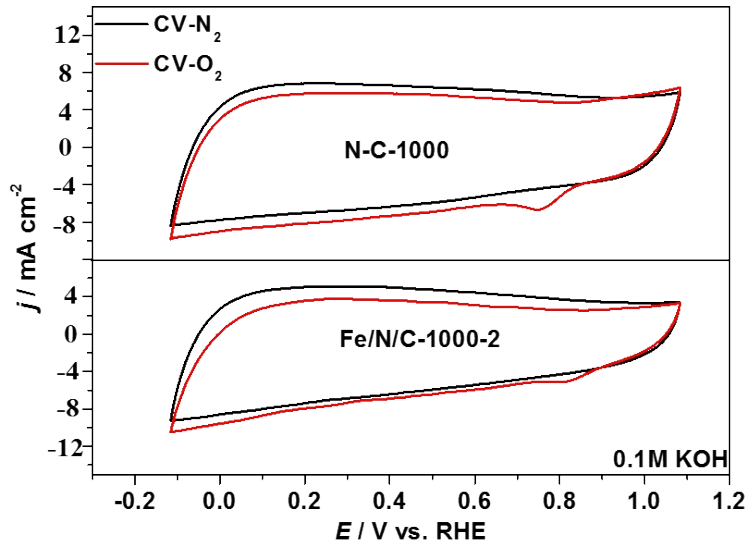

Fig. S17. CV curves of N-C-1000 and Fe/N/C-1000-2 in N_2- and O_2-saturated 0.1 M KOH.

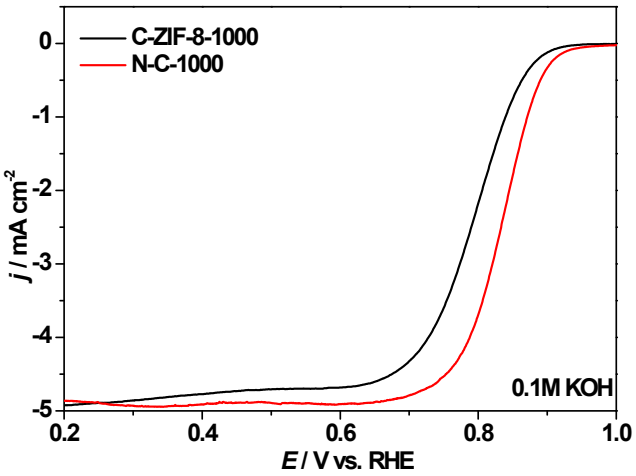

Fig. S18. ORR polarization curves of C-ZIF-8-1000 and N-C-1000 in O_2-saturated 0.1 M KOH electrolyte.

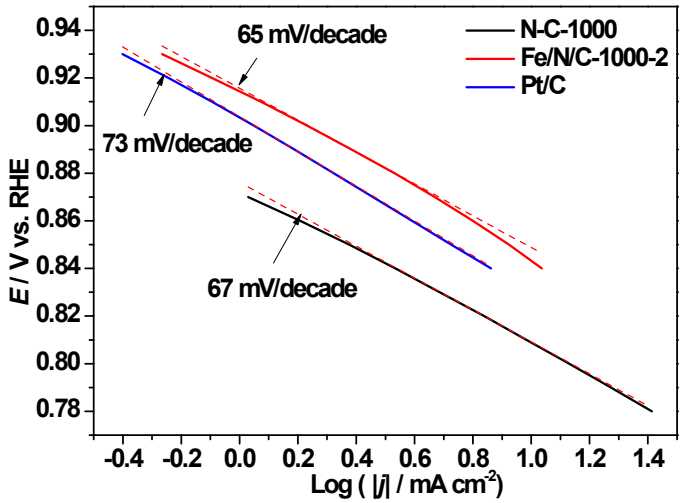

Fig. S19. Corresponding Tafel plots of N-C-1000, Fe/N/C-1000-2 and Pt/C in O_2-saturated 0.1M KOH electrolyte.

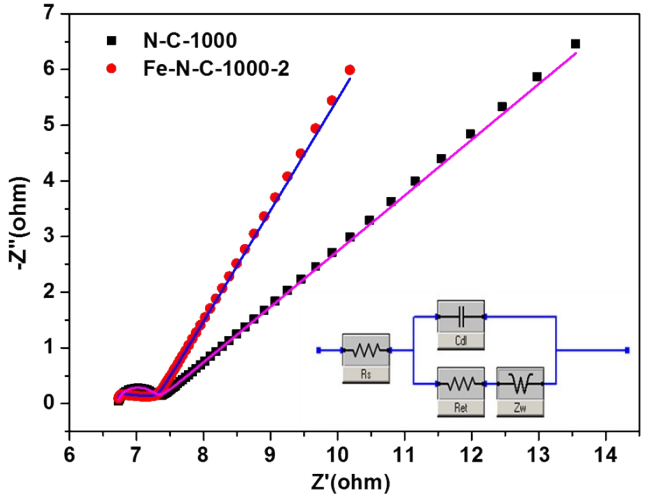

Fig. S20. Nyquist plots for N-C-1000, Fe/N/C-1000-2 loaded on glass-carbon electrodes in O_2-saturated 0.1 M KOH solution.

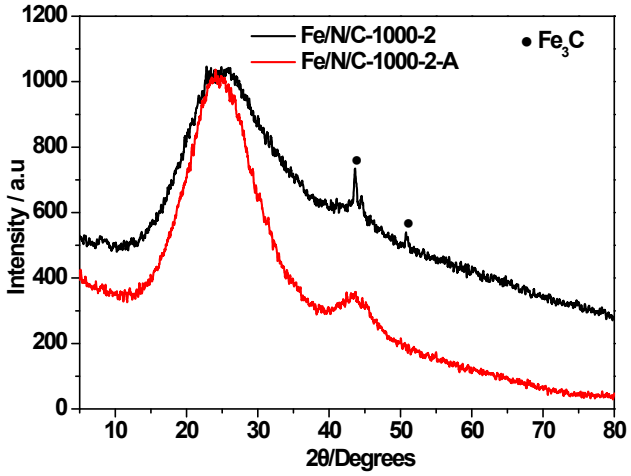

Fig. S21. PXRD patterns of Fe/N/C-1000-2 and Fe/N/C-1000-2-A.

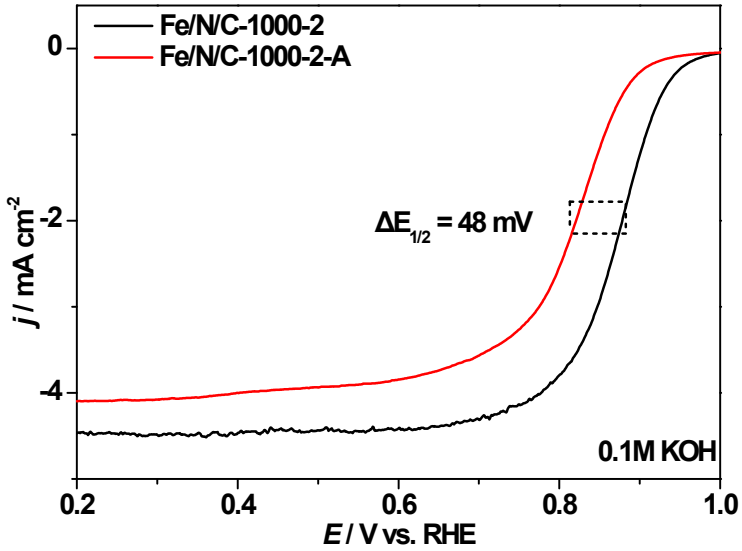

Fig. S22. LSVs of ORR on the Fe/N/C-1000-2 and Fe/N/C-1000-2-A.

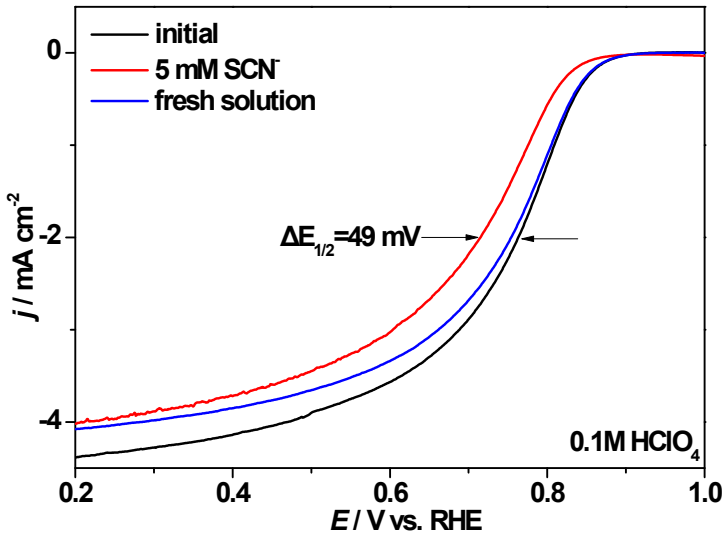

Fig. S23. Effects of SCN^- on ORR activity for Fe/N/C-1000-2 in O_2-saturated 0.1 M $HClO_4$ electrolyte.

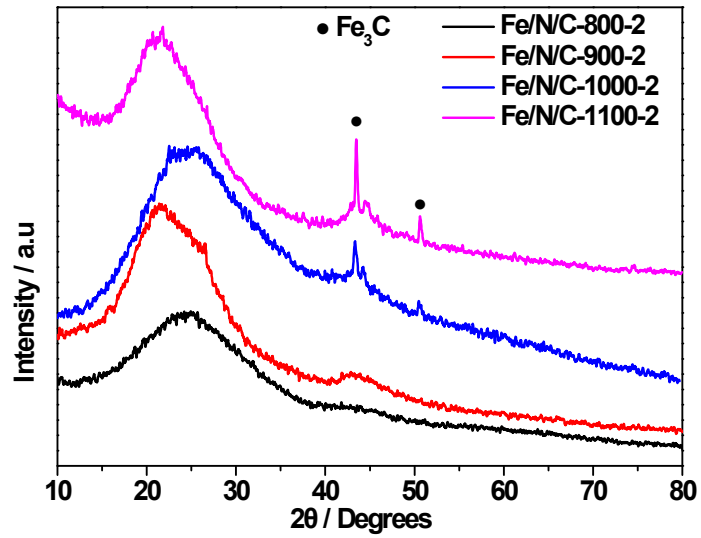

Fig. S24. PXRD patterns of Fe/N/C-T-2 (T= 800, 900, 1000 and 1100).

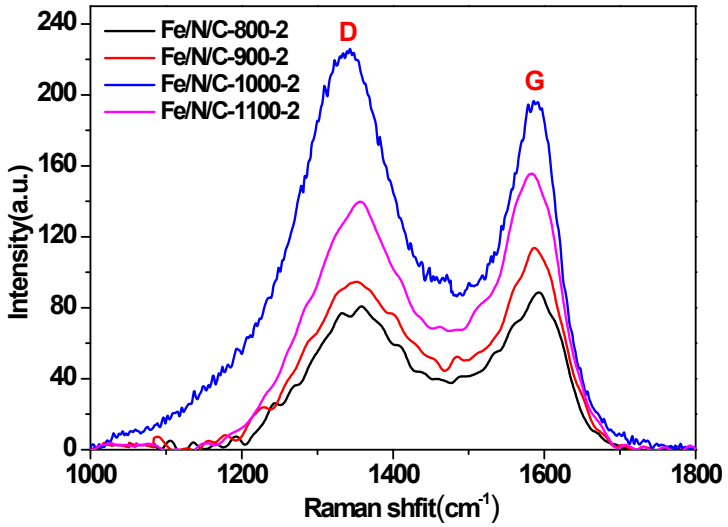

Fig. S25. Raman spectra of Fe/N/C-T-2 (T= 800, 900, 1000 and 1100).

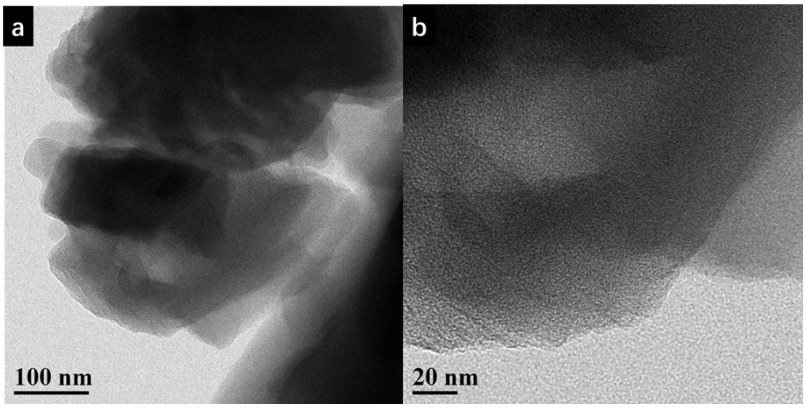

Fig. S26. HRTEM image of Fe/N/C-800-2.

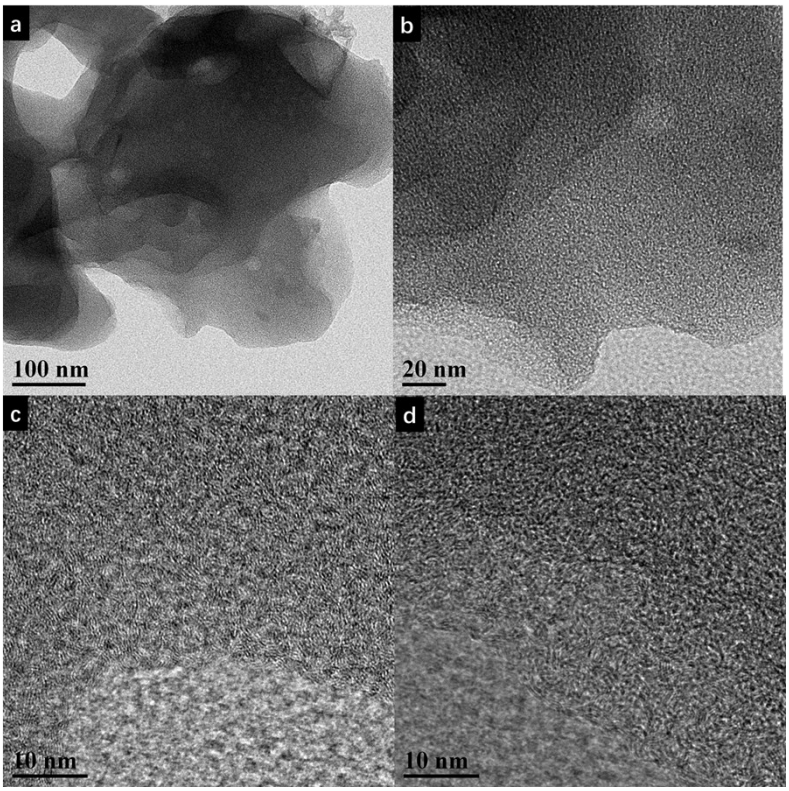

Fig. S27. HRTEM image of Fe/N/C-900-2

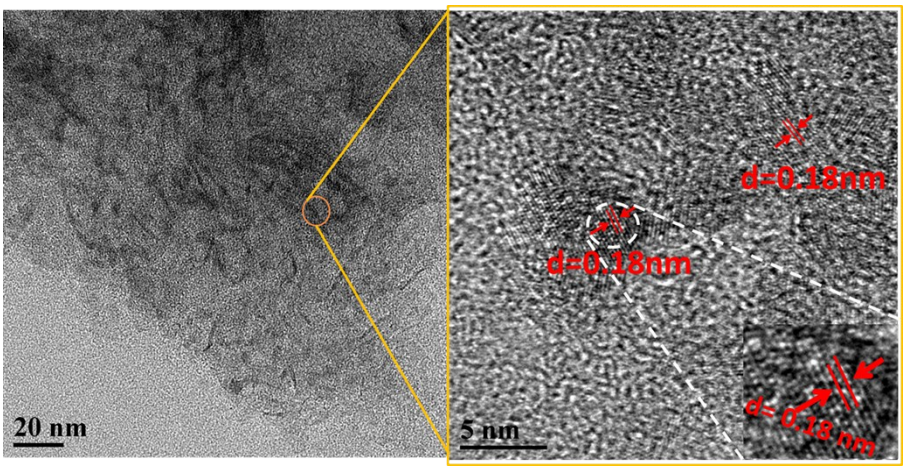

Fig. S28. HRTEM image of Fe/N/C-1100-2.

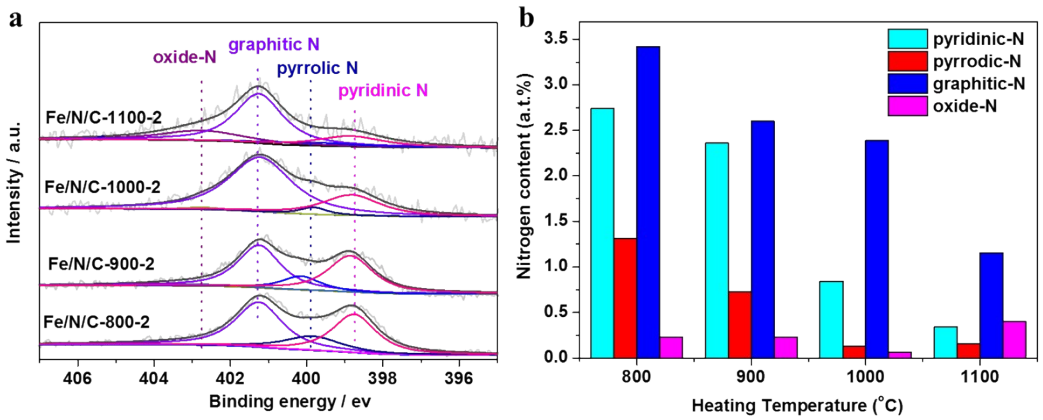

Fig. S29. (a) Evolution of XPS N1s spectra of the Fe/N/C catalyst with increasing heating temperature 800 °C up to 1100 °C; (b) N species percentage of Fe/N/C-T-2 (T= 800, 900, 1000 and 1100) determined by XPS measurements.

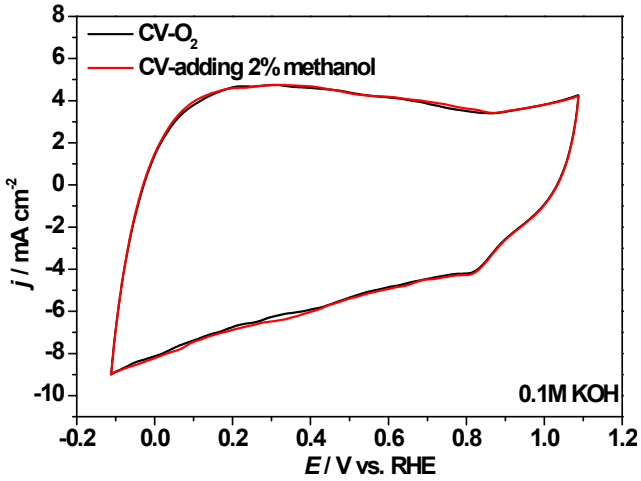

Fig. S30. Methanol tolerance test in O_2-saturated 0.1 M KOH solution for Fe/N/C-1000-2.

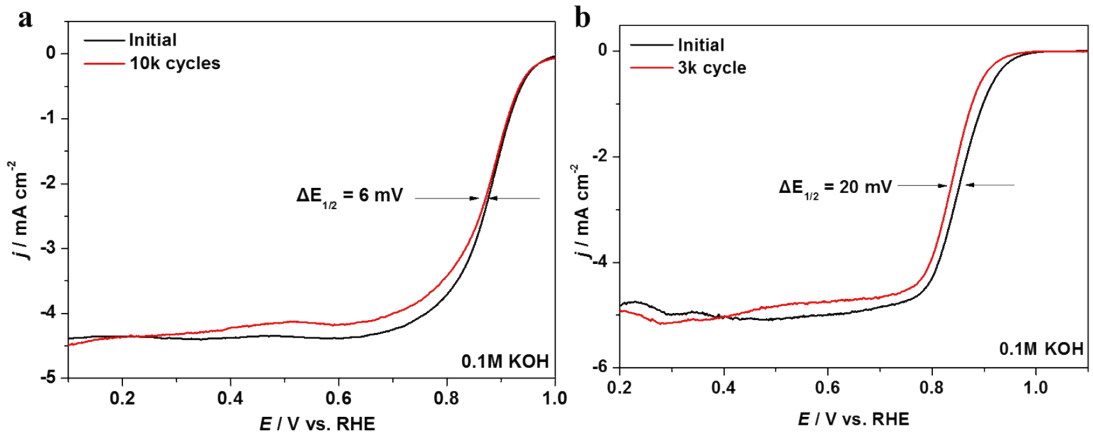

Fig. S31. (a) The polarization curves of ORR on Fe/N/C-1000-2 before and after a 10000-cycle ADT in O_2-saturated 0.1M KOH electrolyte; (b)The polarization curves of ORR on Pt/C before and after a 3000-cycle ADT in O_2-saturated 0.1M KOH electrolyte.

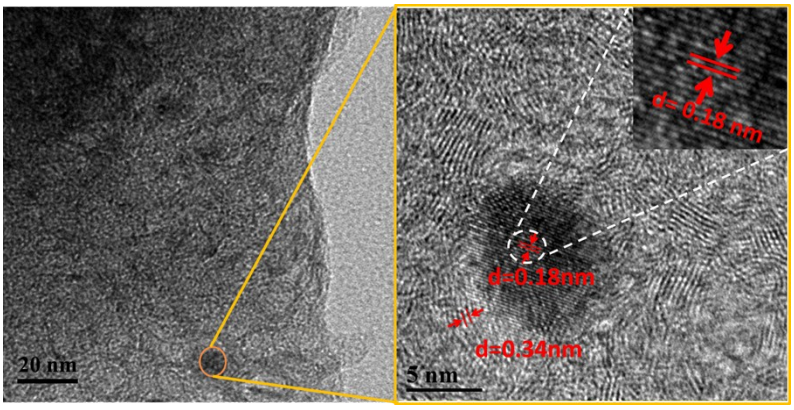

Fig. S32. HRTEM images of Fe/N/C-1000-2 after 10,000 cycles in 0.1 M KOH.

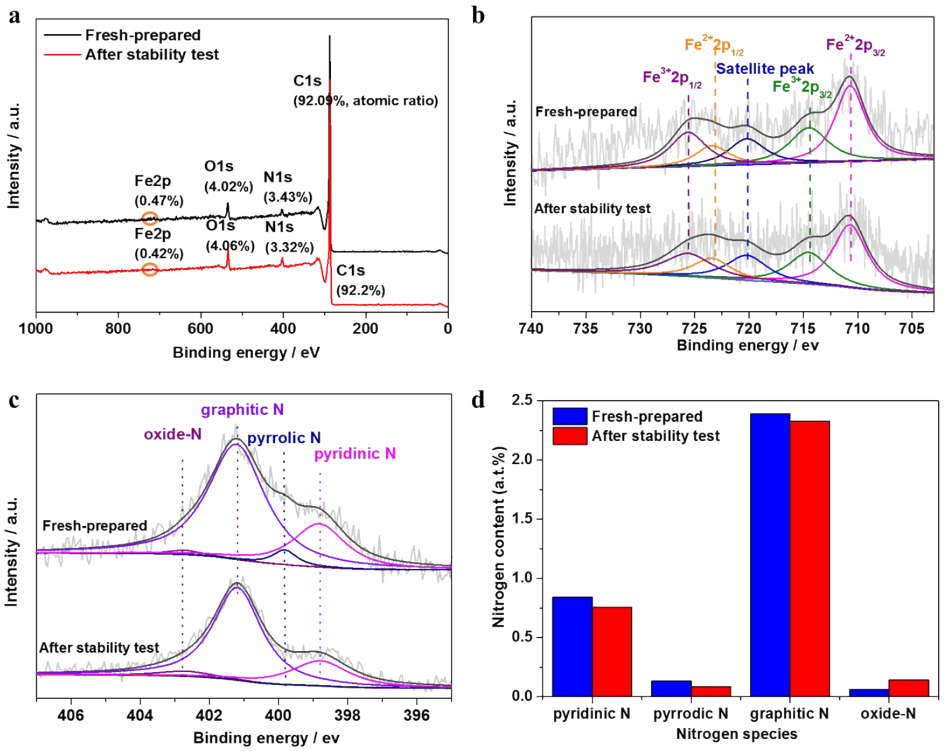

Fig. S33. (a) XPS survey spectra, (b) Fe 2p spectra, (c) N 1s XPS spectra and (d) N species percentage of Fe/N/C-1000-2 before and after 10000 potential cycles in 0.1 M KOH.

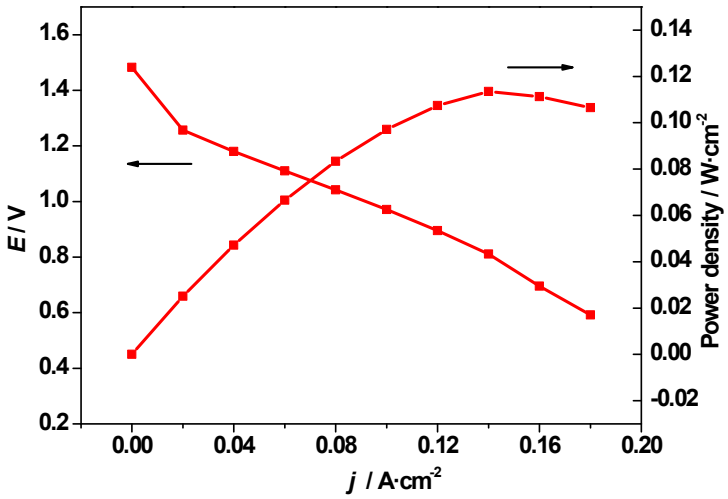

Fig. S34. Discharge polarization curves and corresponding power densities of the primary Zn–air battery based on Fe/N/C-1000-2.

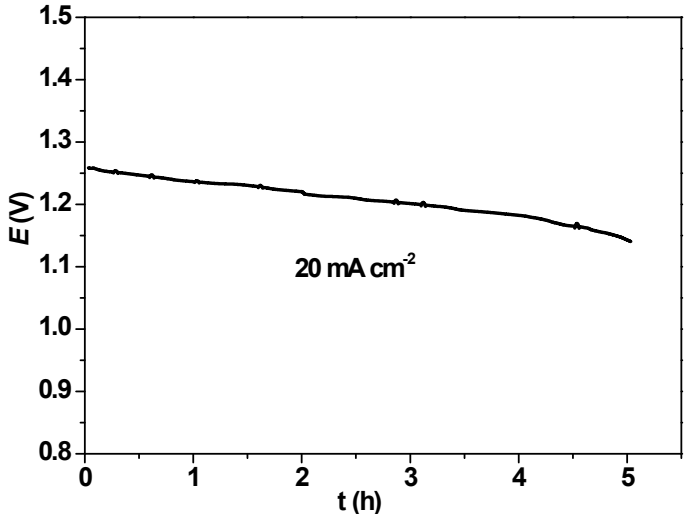

Fig. S35. Discharge curves of the primary Zn–air batteries with Fe/N/C-1000-2 as the ORR catalyst and the KOH electrolyte at 20 mA cm^{-2}.

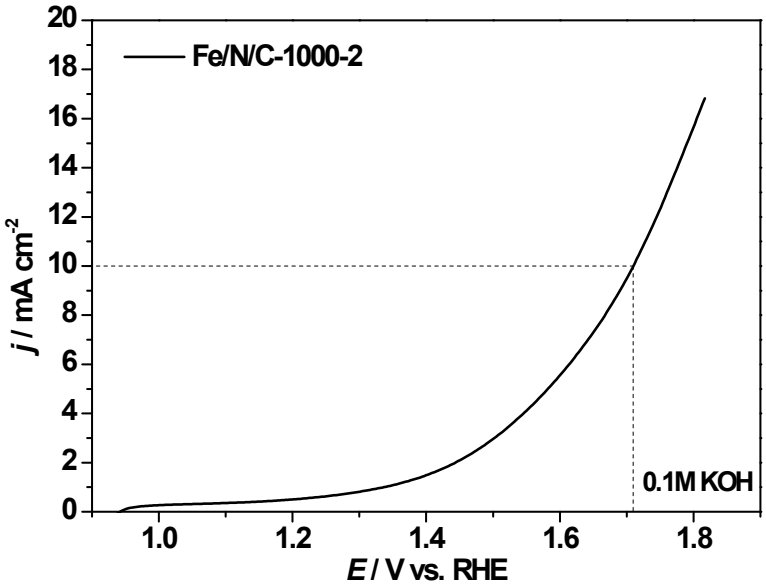

Fig. S36. OER polarization curve of Fe/N/C-1000-2. (Fe/N/C-1000-2 exhibits the poor OER performance with a potential of 1.71 V (vs. RHE) at 10 mA cm^{-2}.)

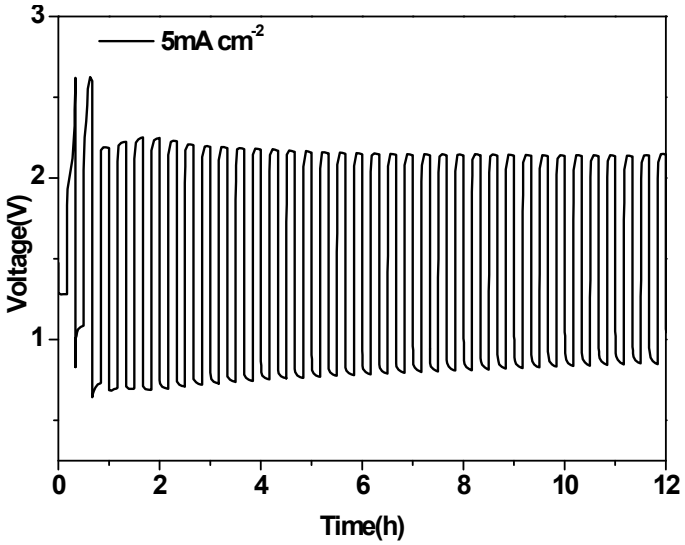

Fig. S37. The charge-discharge cycling curves of the Zn-air cell with Fe/N/C-1000-2 at 5 mA cm^{-2}. (In the first two circles, a higher charging voltage (2.62 V) is observed. Although the charging voltage drops to a reasonable voltage range (2.19 V) from the third circle and maintains within 12 hrs, the discharging voltage is too low (0.71 V).)

Fig. S38. Photograph of the Zn–air battery with Fe/N/C-1000-2 catalyst.

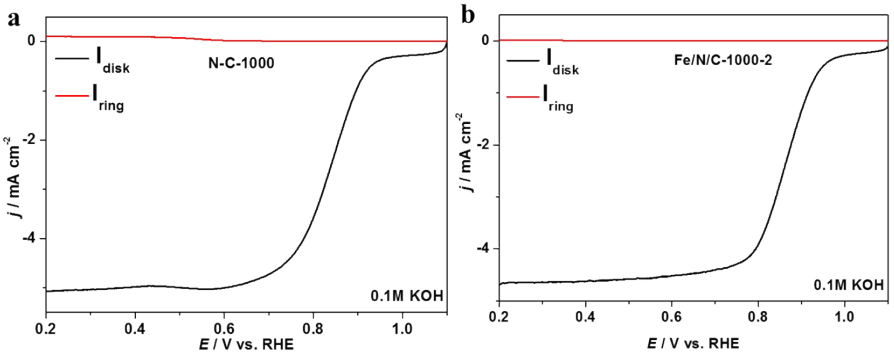

Fig. S39. The RRDE curve of (a) N-C-1000 and (b) Fe/N/C-1000-2 in 0.1M KOH at a rotating rate of 1600 rpm.

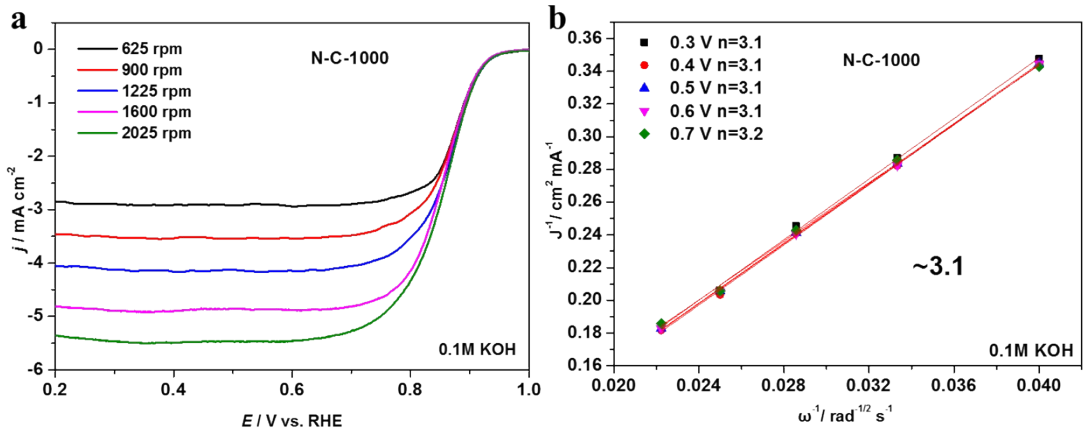

Fig. S40. (a)K–L plots derived from LSVs of ORR on N-C-1000 (0.6 mg cm^{-2}) at various rotating speeds in 0.1 M KOH solution; (b) K–L plots derived from LSVs of ORR on N-C-1000 at K–L plots of j^{-1} versus $\omega^{-1/2}$ in 0.1 M KOH solution.

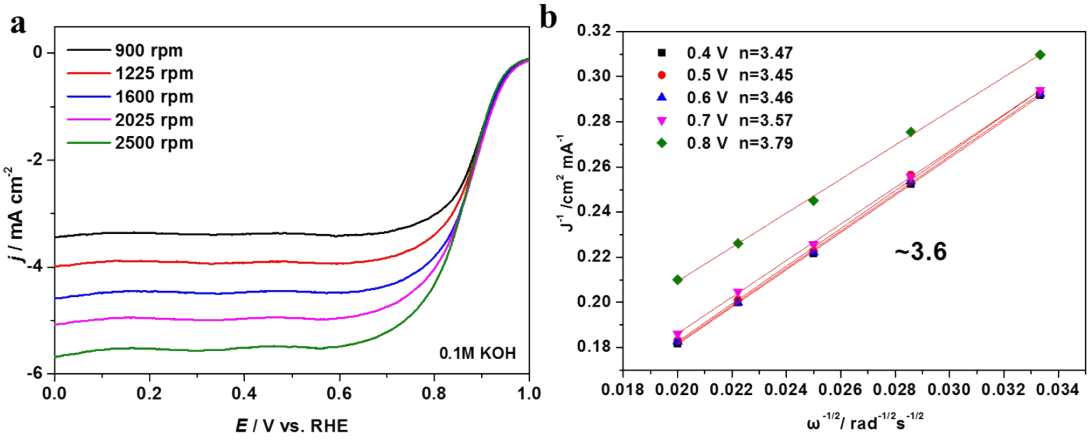

Fig. S41. (a)K–L plots derived from LSVs of ORR on Fe/N/C-1000-2 (0.6 mg cm^{-2}) at various rotating speeds in 0.1 M KOH solution; (b) K–L plots derived from LSVs of ORR on Fe/N/C-1000-2 at K–L plots of j^{-1} versus $\omega^{-1/2}$ in 0.1 M KOH solution.

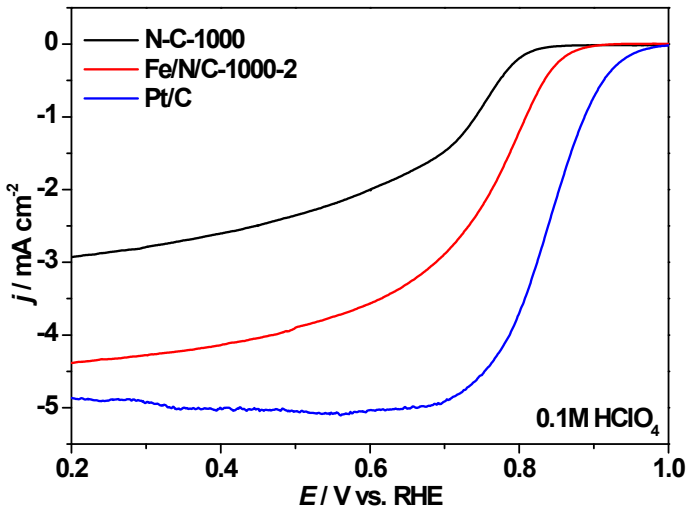

Fig. S42. ORR polarization curves of N-C-1000, Fe/N/C-1000-2 and Pt/C in O_2-saturated 0.1M $HClO_4$ electrolyte. (In acidic media, Fe/N/C-1000-2 likewise delivers a better ORR catalytic activity

(E_{onset} = 0.89; $E_{1/2}$ = 0.76 V vs. RHE) than N-C-1000 (E_{onset} = 0.85; $E_{1/2}$ = 0.70 V vs RHE))

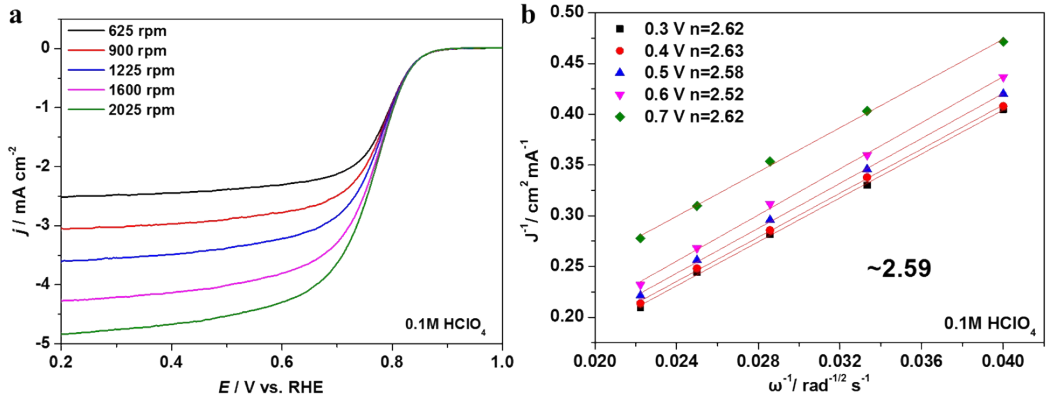

Fig. S43. (a)K–L plots derived from LSVs of ORR on Fe/N/C-1000-2 (0.6 mg cm^{-2}) at various rotating speeds in 0.1 M $HClO_4$ solution; (b) K–L plots derived from LSVs of ORR on Fe/N/C-1000-2 at K–L plots of j^{-1} versus $\omega^{-1/2}$ in 0.1 M $HClO_4$ solution. (The electron transfer number in acidic solution is ca. 2.59, suggesting a dominant 2-e^- ORR pathway.)

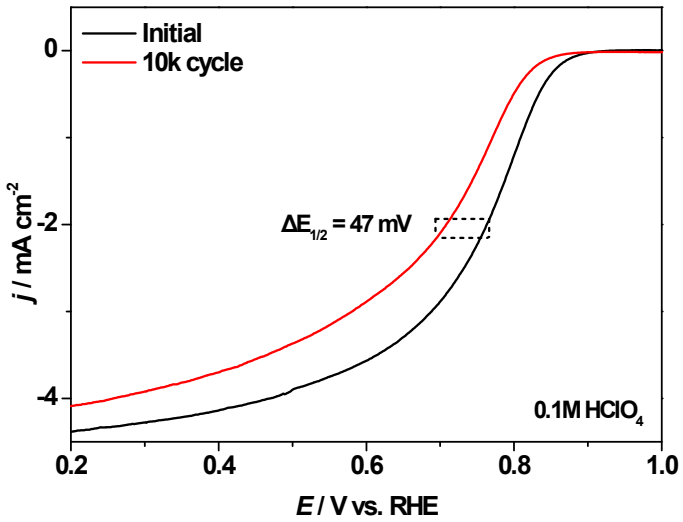

Fig. S44. The polarization curves of ORR on Fe/N/C-1000-2 before and after a 10000-cycle ADT in O_2-saturated 0.1M $HClO_4$ electrolyte. (A remarkable negative shift of $E_{1/2}$ (ca. 47 mV) was observed after a 10000-cycle ADT (accelerated duration test), largely due to the instability of Fe_3C in acidic media.)

Table S2 Elemental qualification of Fe/N/C catalysts as function of heating temperatures.

Sample	N at%	Fe at%	O at%	C at%
Fe/N/C-800-2	7.72	0.36	8.49	83.43
Fe/N/C-900-2	6.05	0.31	7.7	85.94
Fe/N/C-1000-2	3.43	0.47	4.02	92.09
Fe/N/C-1100-2	2.1	0.34	3.64	93.92

Table S3 Comparison of the E_{onset} and $E_{1/2}$ toward ORR for non-noble metal catalysts reported and this work in 0.1 M KOH.

Catalyst	E_{onset} vs RHE	$E_{1/2}$ vs RHE	n [a)]	Loading mass (μg·cm^{-2})	References

Fe/N/C-1000-2	1.0	0.87	3.95	600	This work
FePhen@MOF-ArNH_3	1.03	0.86	/	600	2
FeN_x-PNC	0.997	0.86	≈4	140	3
N-Fe/CNs-700-800-NH_3	0.93	0.859	3.7	100	4
FeNS-PC-800	0.95	0.85	≈3.8	342	5
Fe/SNC	0.97	0.85	/	600	6
3D Co/NCNTs-Zn/Co	0.969	0.84	/	500	7
Fe−N-SCCFs	1.03	0.883	3.9	614	8
Co@N-CNTs-m	0.929	0.849	3.6	600	9

[a)] the electron transfer numbers (n) were calculated from the RRDE voltammograms.

Table S4 Comparison of Zn-air batteries performance of this work with recently reported highly active catalytic materials.

Catalyst	Open potential (V)	Power Density (mW cm^{-2})	References
Fe/N/C-1000-2	1.43	113	This work
Fe@C-NG/NCNTs	1.37	101.3	10
FeNx/C-700-20	≈1.6	36	11
FeNi-NC	1.3	80.8	12
NiFe@NCX	1.35	80	13
Ni3Fe-Co9S8/rGO	1.4	125	14
C-MOF-C2-900	1.46	105	15
N-GCNT/FeCo-3	1.48	97.6	16
Pt/C + Ir/C	1.42	73.4	17

Notes and references

1. H.-B. Zhu and Z.-Y. Sun, *Inorganic Chemistry Communications*, 2018, **96**, 202-205.
2. K. Strickland, E. Miner, Q. Jia, U. Tylus, N. Ramaswamy, W. Liang, M.-T. Sougrati, F. Jaouen and S. Mukerjee, *Nature communications*, 2015, **6**, 7343.
3. L. Ma, S. Chen, Z. Pei, Y. Huang, G. Liang, F. Mo, Q. Yang, J. Su, Y. Gao and J. A. Zapien, *ACS nano*, 2018, **12**, 1949-1958.
4. S. Li, C. Cheng, H. W. Liang, X. Feng and A. Thomas, *Advanced Materials*, 2017, **29**, 1700707.
5. Y. Wang, N. Guo, L. Zhu, Y. Pan, R. Wang, Z. Zhang and S. Qiu, *Chemical Communications*, 2018, **54**, 12974-12977.
6. P. Chen, T. Zhou, L. Xing, K. Xu, Y. Tong, H. Xie, L. Zhang, W. Yan, W. Chu and C. Wu, *Angewandte Chemie International Edition*, 2017, **56**, 610-614.
7. X. Wan, R. Wu, J. Deng, Y. Nie, S. Chen, W. Ding, X. Huang and Z. Wei, *Journal of Materials Chemistry A*, 2018, **6**, 3386-3390.
8. B. Wang, X. Wang, J. Zou, Y. Yan, S. Xie, G. Hu, Y. Li and A. Dong, *Nano letters*, 2017, **17**, 2003-2009.
9. S. Zhang, Y. Zhang, W. Jiang, X. Liu, S. Xu, R. Huo, F. Zhang and J.-S. Hu, *Carbon*, 2016, **107**, 162-170.
10. Q. Wang, Y. Lei, Z. Chen, N. Wu, Y. Wang, B. Wang and Y. Wang, *Journal of Materials*

Chemistry A, 2018, **6**, 516-526.
11. S. Han, X. Hu, J. Wang, X. Fang and Y. Zhu, *Advanced Energy Materials*, 2018, **8**, 1800955.
12. L. Yang, X. Zeng, D. Wang and D. Cao, *Energy Storage Materials*, 2018, **12**, 277-283.
13. J. Zhu, M. Xiao, Y. Zhang, Z. Jin, Z. Peng, C. Liu, S. Chen, J. Ge and W. Xing, *ACS Catalysis*, 2016, **6**, 6335-6342.
14. X. Hu, T. Huang, Y. Tang, G. Fu and J.-M. Lee, *ACS applied materials & interfaces*, 2019, **11**, 4028-4036.
15. M. Zhang, Q. Dai, H. Zheng, M. Chen and L. Dai, *Advanced Materials*, 2018, **30**, 1705431.
16. C. Y. Su, H. Cheng, W. Li, Z. Q. Liu, N. Li, Z. Hou, F. Q. Bai, H. X. Zhang and T. Y. Ma, *Advanced Energy Materials*, 2017, **7**, 1602420.
17. L. Li, J. Yang, H. Yang, L. Zhang, J. Shao, W. Huang, B. Liu and X. Dong, *ACS Applied Energy Materials*, 2018, **1**, 963-969.